

# Super-LIO: A Robust and Efficient LiDAR-Inertial Odometry System with a Compact Mapping Strategy

Liansheng Wang<sup>1</sup>, Xinkle Zhang<sup>1</sup>, Chenhui Li<sup>2</sup>, Dongjiao He<sup>3</sup>, Yihan Pan<sup>1</sup>, Jianjun Yi<sup>1†</sup>

**Abstract**—LiDAR-Inertial Odometry (LIO) is a foundational technique for autonomous systems, yet its deployment on resource-constrained platforms remains challenging due to computational and memory limitations. We propose Super-LIO, a robust LIO system that demands both high performance and accuracy, ideal for applications such as aerial robots and mobile autonomous systems. At the core of Super-LIO is a compact octo-voxel-based map structure, termed OctVox, that limits each voxel to eight fused subvoxels, enabling strict point density control and incremental denoising during map updates. This design enables a simple yet efficient and accurate map structure, which can be easily integrated into existing LIO frameworks. Additionally, Super-LIO designs a heuristic-guided KNN strategy (HKNN) that accelerates the correspondence search by leveraging spatial locality, further reducing runtime overhead. We evaluated the proposed system using four publicly available datasets and several self-collected datasets, totaling more than 30 sequences. Extensive testing on both X86 and ARM platforms confirms that Super-LIO offers superior efficiency and robustness, while maintaining competitive accuracy. Super-LIO processes each frame approximately 73% faster than SOTA, while consuming less CPU resources. The system is fully open-source and plug-and-play compatible with a wide range of LiDAR sensors and platforms. The implementation is available at: <https://github.com/Liansheng-Wang/Super-LIO.git>.

**Index Terms**—LiDAR-Inertial Odometry, Real-Time Robotics, Resource-Constrained Systems

## I. INTRODUCTION

LiDAR-Inertial Odometry (LIO) is a key component of modern autonomous navigation systems, combining the geometric precision of LiDAR with the high-frequency motion priors from inertial measurement units (IMUs) to achieve outstanding accuracy and robustness. It has been widely deployed in mobile robots [1], unmanned aerial vehicles (UAVs) [2], and autonomous driving [3]. However, deploying LIO on low-power, resource-constrained platforms remains challenging, as it requires balancing accuracy, real-time responsiveness, computational efficiency, and memory footprint, while it ultimately serves as a low-level localization module underpinning higher-level tasks such as exploration [4], language-driven navigation [5], and multi-agent coordination [6], where its value lies in delivering reliable pose estimation with minimal latency and computational cost.

Early LiDAR Simultaneous Localization and Mapping (SLAM) systems, such as LOAM [7] and LeGO-LOAM [8], decomposed the SLAM pipeline into feature extraction, frame-to-frame registration, and map maintenance, establishing the

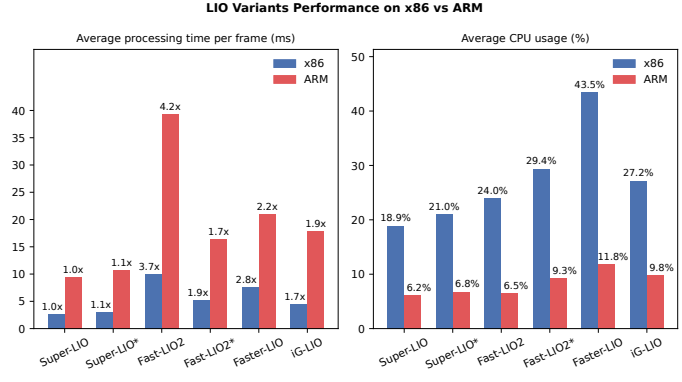


Fig. 1. Performance comparison of different LIO methods on X86 and ARM platforms. The left plot shows the average processing time per LiDAR frame, annotated relative to Super-LIO (1x) on each platform, while the right plot shows runtime CPU utilization. Note that the X86 experiments were conducted with 5x playback speed, which results in noticeably higher CPU usage compared to ARM.

foundation for modern LIO. LIO-SAM [9] introduced an incremental pose graph optimization backend based on GT-SAM [10], enabling multisensor fusion and global consistency through loop closure. More recent systems, including HAB [11] and Voxel-SLAM [12], incorporated hierarchical global optimization to reduce accumulated drift and improve map quality. While these optimization-based frameworks excel in map fidelity, their iterative solvers scale poorly with map size, resulting in high computational overhead and limited suitability for real-time applications on resource-limited hardware.

In contrast, filtering-based frameworks have emerged as a practical alternative for applications requiring low latency and stable performance. FAST-LIO [13] introduced a tightly coupled LiDAR-IMU fusion architecture using an error-state Kalman filter, while FAST-LIO2 [14] removed explicit feature extraction and leveraged an incremental KD-tree (iKD-tree) for efficient nearest-neighbor queries. Faster-LIO [15] replaced the iKD-tree with a sparse hash-voxel map (iVox) and adopted aggressive parallelization to further improve throughput, albeit at the cost of higher instantaneous computational demand. Point-LIO [16] extended FAST-LIO2 with point-wise state updates, significantly enhancing robustness in high-dynamic scenarios. These systems generally store raw points in the map and use point-to-plane constraints, requiring density control mechanisms to keep K-Nearest Neighbor (KNN) search and planar fitting tractable.

Beyond raw-point maps, VoxelMap [17] introduced a parametric plane-based representation with octree indexing to facilitate local planar feature extraction. iG-LIO [18] drew inspiration from VGICP [19] and stored normalized covariance matrices within hashed voxels, encoding structural informa-

<sup>†</sup>Corresponding author: Jianjun Yi (jjyi@ecust.edu.cn)

<sup>1</sup> School of Mechanical and Power Engineering, East China University of Science and Technology, Shanghai, China.

<sup>2</sup> Shanghai Artificial Intelligence Laboratory, Shanghai, China.

<sup>3</sup> The University of Hong Kong (HKU)

tion without retaining raw points. While this design reduces storage, its reliance on repeated matrix decompositions and inversions can hinder performance on ARM-based platforms with limited floating-point capability. Liv-GS [20] and GS-LIVO [21] took this further by modeling point-cloud distributions as Gaussian primitives, enabling high-fidelity surface modeling but often requiring GPU acceleration due to their computational complexity.

In this work, we exploit the potential of high-frequency, accurate LiDAR depth measurements and revisit the LIO mapping pipeline to further improve efficiency and free computational resources for downstream tasks. We propose **Super-LIO**, a robust and efficient system that leverages a sparse hash-voxel structure [15] together with a compact octo-voxel-based representation, termed OctVox. Each voxel is subdivided into eight subvoxels, each storing an incrementally averaged point, enabling global noise suppression and density regularization without increasing hash table complexity. We further introduce a heuristic-guided KNN (HKNN) strategy that leverages precomputed relative neighbor patterns exploiting subvoxel octant symmetry. Evaluations on four public and self-collected datasets (30+ sequences, over 400 minutes) across x86 (AMD 5800H) and ARM (NVIDIA Orin NX) platforms show that Super-LIO matches the accuracy of state-of-the-art systems while significantly reducing computational load (see Fig. 1). The main contributions are:

- We propose a compact octo-voxel-based map representation (OctVox), where each voxel contains eight incrementally averaged subvoxels, achieving density regularization and global noise suppression without storing raw points.
- We design a heuristic-guided KNN strategy that exploits subvoxel octant symmetry and unified query templates to improve neighbor quality and query efficiency.
- We conduct comprehensive evaluations on diverse datasets and hardware platforms, demonstrating that Super-LIO achieves superior runtime efficiency, low CPU usage, and high robustness.
- We will release the full system to benefit the research community.

## II. RELATED WORKS

This section reviews prior LIO systems with an emphasis on the design choices in their mapping modules and correspondence search strategies, which are the primary computational bottlenecks in real-time deployment.

**LIO frameworks.** Optimization-based LIO systems [9], [11], [12], [22] typically aim for global consistency via pose graph optimization or hierarchical bundle adjustment. These methods can achieve low long-term drift but suffer from scalability issues: their iterative nonlinear solvers scale poorly with map size, and runtime grows with the number of accumulated keyframes.

Filtering-based LIO frameworks [14]–[16] maintain a bounded state vector and fixed-lag window, ensuring constant per-frame estimation complexity regardless of mapping duration. FAST-LIO2 [14] removed explicit feature extraction and introduced the iKD-Tree for efficient point association. Faster-LIO [15] replaced the iKD-tree with a sparse hash-voxel map,

yielding average  $O(1)$  voxel access and improving cache locality by restricting neighbor stencils and scanning contiguous voxel buckets, while throughput is further boosted via parallelization. Point-LIO [16] increased observation bandwidth by updating the state with every valid point-to-plane constraint, improving robustness under aggressive motion. All of these systems follow the error-state Kalman filter formulation on manifolds [23], with extensions such as SI-LIO [24] adopting the invariant EKF [25] to improve linearization consistency. In most cases, the majority of runtime is consumed not by the filter update itself but by the map management and KNN search modules, which is precisely the focus of this work.

**Map structures and efficiency.** Map structures for LIO differ in their spatial indexing strategies. KD-trees provide  $O(\log N)$  query complexity but require frequent rebuilding in incremental mapping, introducing  $O(N \log N)$  update cost over time. iKD-Tree [14] mitigates the rebuild overhead by supporting online insertion, but still suffers from  $O(\log N)$  amortized update cost and pointer-heavy traversals, which can reduce cache efficiency on modern CPUs. Octrees [22], [26], [27] reduce memory by hierarchical subdivision, but high resolution demands deep trees, increasing pointer traversal cost and reducing cache efficiency.

Hashing-based voxel maps [15] scale well with environment size and support  $O(1)$  average voxel access, though KNN efficiency depends on the per-voxel point count. KISS-ICP [28] uses a similar hash-voxel grid but caps the number of stored points per voxel and applies range filtering to bound map size, offering predictable memory and query cost but offering limited control over spatial density distribution. Adaptive-LIO [29] extends this design to multi-resolution hash maps selected dynamically according to scene openness, improving adaptability at the expense of extra memory and neighbor search overhead. Probabilistic voxel methods [18], [19], [30] replace raw points with compact statistical models, avoiding explicit KNN queries but relying on fixed-resolution voxelization, which limits adaptability to varying scene scales. Repeated covariance computations can also suffer from numerical precision loss on ARM-class processors, potentially degrading registration accuracy.

Our approach follows the hashing paradigm but applies an octant subdivision within each voxel, storing one incrementally averaged point per subvoxel to decrease the computation complexity. This ensures constant per-voxel memory usage, enforces point density bounds, and suppresses noise without increasing hash table complexity.

**KNN strategies and complexity.** In incremental LIO, the cost of KNN search comes from generating candidates and selecting the  $k$  nearest ones. KD-trees (including iKD-tree [14]) typically achieve  $O(\log N + k)$  query complexity with  $O(\log N)$  amortized insertion, but pointer traversal and rebalancing can hurt cache performance. Hash-based voxel maps [15] reduce indexing to  $O(1)$  on average, so the runtime mainly depends on the number of points checked within the voxel neighborhood. This number is affected by both the neighborhood size and the per-voxel storage cap; for example, KISS-ICP [28] limits each voxel to  $N_{\max}$  points. Faster-LIO [15] restricts the search to only adjacent voxels for speed, but this can reduce neighbor quality

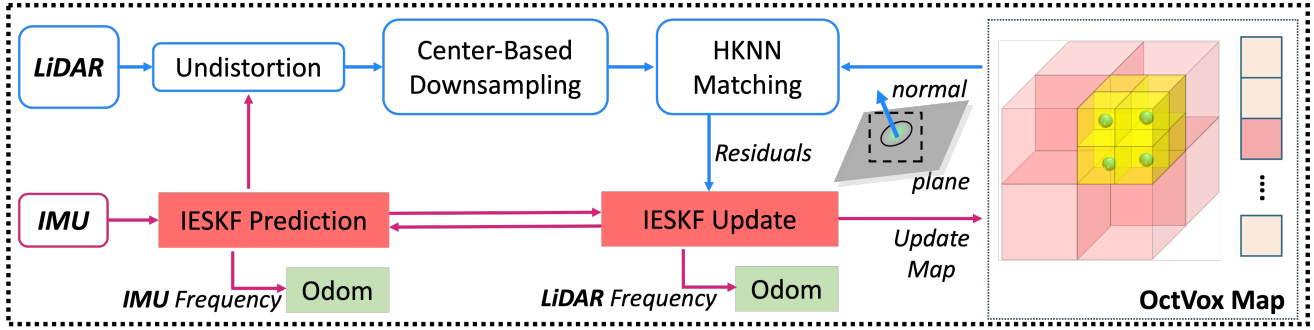


Fig. 2. Overview of Super-LIO. An IESKF fuses IMU and LiDAR data: IMU measurements propagate the state at the IMU rate; at each LiDAR frame, points are de-skewed using the IMU state, center-based downsampled, and, via a heuristic-guided KNN (HKNN) in the OctVox Map, nearest neighbors are retrieved to construct point-to-plane residuals. These residuals feed the IESKF observation update. The map stores up to eight subvoxel representatives per voxel and is updated online to ensure efficient and accurate correspondences.

in sparse areas.

Our method expands the neighborhood search using a precomputed near-to-far traversal order that exploits octant symmetry within each voxel. With an early-termination rule, this design improves neighbor quality without significantly increasing the number of points that need to be examined.

### III. METHOD

#### A. System Overview

As shown in Fig. 2, Super-LIO is a tightly coupled LiDAR–IMU odometry that follows an iterated error-state Kalman filter (IESKF) formulation [13], while introducing two efficiency-centric modules: (i) OctVox, a sparse hash map that stores at most eight incrementally averaged representatives per voxel for explicit density control and incremental denoising (Sec. III-C); and (ii) a HKNN correspondence module that exploits subvoxel octant symmetry and a near-to-far subvoxel traversal order to restrict neighbor search to a small local neighborhood (Sec. III-D). After IMU-aided de-skewing, each scan is downsampled via a center-based selection strategy that better preserves spatial distribution than standard voxel filters; the selected points are then used both to form scan-to-map point-to-plane residuals for IESKF and to update the OctVox map.

#### B. State and Notation

Let  $\mathcal{G}$ ,  $\mathcal{L}$ , and  $\mathcal{I}$  denote the Global, LiDAR, and IMU frames, respectively. The LiDAR–IMU extrinsic transform  $\mathbf{T}_{\mathcal{L}}^{\mathcal{I}} = (\mathbf{R}_{\mathcal{L}}^{\mathcal{I}}, \mathbf{p}_{\mathcal{L}}^{\mathcal{I}})$  is assumed to be well calibrated and fixed. The system state at time  $t$  is defined as Eq.(1).

$$\mathbf{X}_t \triangleq \left[ \mathbf{R}_{\mathcal{I}}^{\mathcal{G}}, \mathbf{p}_{\mathcal{I}}^{\mathcal{G}}, \mathbf{v}_{\mathcal{I}}^{\mathcal{G}}, \mathbf{b}_a, \mathbf{b}_g, \mathbf{g}^{\mathcal{G}} \right]^{\top} \in SO(3) \times \mathbb{R}^{15}. \quad (1)$$

We denote estimates with a hat ( $\hat{\cdot}$ ) and use superscripts  $(\cdot)^- / (\cdot)^+$  for priori and posteriori; unless stated otherwise, a bare symbol (e.g.,  $X_t$ ) denotes ground truth.

IMU measurements  $\{\mathbf{a}_i, \omega_i\}$  drive propagation at the IMU rate. We use midpoint integration by averaging adjacent samples to reduce discretization error. For each scan anchored at  $t_k$ , raw LiDAR points are first expressed and de-skewed into the IMU frame at the anchor time  $t_k$ :

$$\mathbf{p}_i^{I_k} = \mathbf{R}_{I_k}^{I_k} \left( \mathbf{R}_{\mathcal{L}}^{\mathcal{I}} \mathbf{p}_i^{\mathcal{L}} + \mathbf{p}_{\mathcal{L}}^{\mathcal{I}} \right) + \mathbf{p}_{I_k}^{I_k}, \quad t_i \in [t_{k-1}, t_k], \quad (2)$$

where  $(\mathbf{R}_{I_k}^{I_k}, \mathbf{p}_{I_k}^{I_k})$  denotes the relative IMU motion from  $t_k$  to  $t_k$  obtained by propagation and subsequent interpolation between IMU samples, for example using a constant–velocity model [7], a constant–acceleration model [14], or a higher-order scheme [31]. This convention is used throughout: de-skewed points are retained in the IMU frame  $I_k$  and mapped to the world using Eq.(3) when needed for association or map update.

$$\mathbf{p}_i^{\mathcal{G}} = \mathbf{R}_{\mathcal{I}}^{\mathcal{G}}(t_k) \mathbf{p}_i^{I_k} + \mathbf{p}_{\mathcal{I}}^{\mathcal{G}}(t_k). \quad (3)$$

Selected points then form scan-to-map point-to-plane residuals for the IESKF observation update [13], while the compact OctVox map supplies correspondence targets.

#### C. Octo-Voxel-Based Map (OctVox)

**Data structure.** We employ a hashed voxel grid with a least-recently-used (LRU) policy for memory management. The map is defined as  $\mathcal{M} = \{\mathcal{V}_i \mid i \in \mathbb{N}\}$ , that is, a collection of voxels. Each voxel  $\mathcal{V}_i$  of edge length  $r_v$  is subdivided into  $2 \times 2 \times 2$  subvoxels  $\mathcal{V}_{i,s}$  of edge length  $r_s = \frac{1}{2}r_v$ . A voxel allocates eight contiguous entries, each storing a representative  $\mu_{i,s} \in \mathbb{R}^3$  and a counter  $n_{i,s}$ . The structure can be expressed as

$$\mathcal{V}_i = \{\mathcal{V}_{i,s} \mid s \in [0, 7]\}, \quad \mathcal{V}_{i,s} = (\mu_{i,s}, n_{i,s}).$$

This contiguous layout enforces an explicit density cap of eight representatives per voxel and achieves noise suppression in the global frame through incremental averaging within each subvoxel. The hash table uses Robin Hood hashing with open addressing [32] and is implemented with `tsl::robin_map` [33], improving cache locality and providing near-constant lookup time. When the memory budget is reached, the LRU policy evicts the least-recently-accessed voxels.

**Voxel indexing and update.** Given a point  $\hat{\mathbf{p}}^{\mathcal{G}} \in \mathbb{R}^3$  in the world frame, we quantize it to subvoxel resolution using Eq.(4) to obtain its parent voxel key  $\mathbf{k} \in \mathbb{Z}^3$  and the local linear subvoxel index  $s \in [0, 7]$ .

$$\begin{aligned} \mathbf{k}^{\text{sub}} &= \left\lfloor \frac{\hat{\mathbf{p}}^{\mathcal{G}}}{r_s} \right\rfloor, \quad \mathbf{k} = \mathbf{k}^{\text{sub}} \gg 1, \\ b_x &= k_x^{\text{sub}} \& 1, \quad b_y = k_y^{\text{sub}} \& 1, \quad b_z = k_z^{\text{sub}} \& 1 \\ s &= b_x \mid (b_y \ll 1) \mid (b_z \ll 2) \end{aligned} \quad (4)$$

Here,  $\&$  and  $|$  denote bitwise AND/OR, while  $<<$  and  $>>$  denote left and right shifts, respectively. Equations (4) therefore provide both the voxel key  $\mathbf{k}$  and the subvoxel index  $s$  in  $O(1)$  time, using bitwise operations without conditional branching.

Once  $(\mathbf{k}, s)$  is determined, the corresponding record  $(\mu_s, n_s)$  is updated incrementally. If the entry is uninitialized, it is set to  $(\hat{\mathbf{p}}^G, 1)$ . Otherwise, if  $\|\hat{\mathbf{p}}^G - \mu_s\|_2 \leq \tau_{\text{merge}}$  and  $n_s \leq n_{\text{max}}$ , the update rule

$$\mu_s \leftarrow \mu_s + \frac{1}{n_s+1} (\hat{\mathbf{p}}^G - \mu_s), \quad n_s \leftarrow n_s + 1, \quad (5)$$

is applied. This corresponds to an unbiased incremental mean update, with the estimation variance asymptotically decreasing as  $1/n_s$ .

This procedure resembles online voxel downsampling in the global frame. It enforces bounded density by maintaining at most one representative per subvoxel, while progressively suppressing measurement noise through averaging. While conceptually simple, the results in Sec. IV-B indicate that this design maintains accuracy.

#### D. Heuristic-Guided KNN Search

A major bottleneck in LiDAR-inertial odometry is the repeated KNN search for scan-to-map residuals. Even with OctVox map that cap per-voxel density, a naive search must examine all representatives within a ball of radius  $R$ . Small  $R$  often yields unstable neighbors in sparse areas, whereas larger  $R$  improves quality but requires visiting  $\Theta((R/r_v)^3)$  voxels, so the candidate set grows cubically with  $R$ . Tree-based indices (e.g., KD-trees) scale as  $O(\log N)$  with map size, but lack the constant-time locality of voxel hashing. To address this, we design an HKNN that groups candidate subvoxels by distance and exploits octant symmetry to unify traversal, enabling efficient and robust correspondence search.

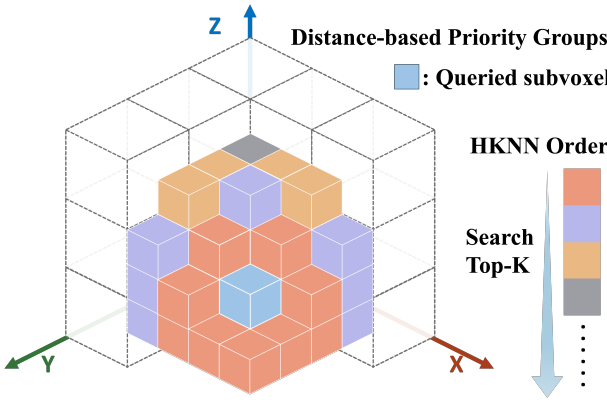


Fig. 3. Illustration of the heuristic KNN candidate selection process based on subvoxel proximity. A query subvoxel (blue) is surrounded by multiple neighboring subvoxels at increasing distances, which are color-coded by their Manhattan distance to the center. These candidates are incrementally inserted into a priority queue and sorted based on their geometric proximity to the query, allowing for an efficient Top-K retrieval.

**HKNN list generation.** As shown in Fig. 3, the HKNN list is defined as an ordered sequence of subvoxel groups, each group contains candidate subvoxels clustered by their spatial distance from the query subvoxel. The list is generated once

during initialization from the maximum search radius and voxel resolution and remains fixed throughout operation. In contrast to conventional neighborhood definitions [15], [17], [18] that require exhaustive traversal of a fixed set, the HKNN list enables group-wise traversal with early termination.

We define each subvoxel as a cube with eight vertices  $\{C_i\}_{i=1}^8$ . Given two subvoxels  $A$  and  $B$ , their distance is defined as the minimum Euclidean distance between their vertex sets, as given in Eq. (6). By definition,  $\text{dis}(A, A) = 0$  and  $\text{dis}(A, B) = \text{dis}(B, A)$ .

$$\text{dis}(A, B) = \min_{C_i \in A, C_j \in B} \|C_i - C_j\|_2. \quad (6)$$

Let  $\mathbf{K} = \{\mathbf{k}_i\}$  denote the set of voxel indices within the maximum search radius  $R_{\text{max}}$ , where each index  $\mathbf{k}_i$  is defined relative to the query voxel center at the origin,  $\mathbf{k}_0 = (0, 0, 0)$ . The corresponding set of subvoxels is given by  $\mathbf{S} = \mathbf{K} \times \{0, \dots, 7\}$ . Accordingly, each element can be expressed as  $\mathbf{S}_{i,j} = (\mathbf{k}_i, s_j)$ .

Due to the discrete nature of the voxel grid, the distances between the reference subvoxel  $\mathbf{S}_{0,0}$  and all subvoxels  $\mathbf{S}_{i,j} \in \mathbf{S}$ , computed by Eq. (6), constitute a finite enumerated set of attainable distances. We denote this set by  $\mathcal{D} = \{d_m \mid m = 0, \dots, M\}$ , which is arranged in ascending order. Subvoxels at the same distance are then grouped into a distance-equivalence set, as defined in Eq. (7), where  $\mathcal{V}(\mathbf{S}_{i,j})$  denotes the cubic region corresponding to subvoxel  $\mathbf{S}_{i,j}$ .

$$\mathcal{H}_m = \{\mathbf{S}_{i,j} \in \mathbf{S} : \text{dis}(\mathcal{V}(\mathbf{S}_{0,0}), \mathcal{V}(\mathbf{S}_{i,j})) = d_m\} \quad (7)$$

Concatenating the groups yields the ordered traversal list defined in Eq. (8).

$$\mathcal{T}(\mathbf{S}_{0,0}) = [\mathcal{H}_0 \parallel \mathcal{H}_1 \parallel \dots \parallel \mathcal{H}_M] \quad (8)$$

Although in the absolute coordinate frame each subvoxel  $\mathbf{S}_{0,j}$  appears to have a distinct traversal list, in the relative coordinate frame all subvoxels share the same search topology. They are related by reflections along the three coordinate axes, a property we term **octant symmetry**. This symmetry implies that the traversal list for any  $\mathbf{S}_{0,j}$  can be obtained from the reference list  $\mathcal{T}(\mathbf{S}_{0,0})$  by a deterministic transformation.

According to the subvoxel indexing rule in Eq. (4), for each entry in the reference traversal list Eq. (8) and for any local subvoxel, the corresponding voxel index and subvoxel index are computed as Eq. (9), where  $(k_x, k_y, k_z, s)$  denotes the entry in  $\mathcal{T}(\mathbf{S}_{0,0})$ ,  $s_j$  is the query subvoxel index,  $(b_x, b_y, b_z)$  are the intermediate variables of  $s_j$  defined in Eq. (4), and  $\oplus$  denotes the bitwise XOR.

$$\mathbf{k}' = ((-1)^{b_x} k_x, (-1)^{b_y} k_y, (-1)^{b_z} k_z), \quad s' = s \oplus s_j. \quad (9)$$

**Heuristic-Guided KNN.** The HKNN search exploits the precomputed priority list in Eq. (8) to accelerate scan-to-map correspondence search. Given a query point, we obtain a global prior via Eq. (3) and restrict the correspondence search in  $\mathcal{M}$  to a fixed neighborhood of radius  $R$ , returning the  $K$  nearest neighbors. The search traverses candidate groups in the pre-computed priority order; occupied subvoxels are evaluated using exact Euclidean distances to their stored representatives, while a bounded max-heap maintains the current top- $K$  neighbors. Upon

**Algorithm 1:** Heuristic-Guided KNN (HKNN)

---

**Input:** Query point  $\mathbf{p}^T$  (IMU frame); prior state  $\hat{X}^-$ ;  
voxel map  $\mathcal{M}$ ; canonical traversal list  $\mathcal{T}(\mathbf{S}_{0,0})$   
Per Eq. (8); group lower bounds  $\mathcal{D} = \{d_m\}_{m=0}^M$ ;  
fixed radius  $R \leq R_{max}$ ; target  $K$

**Output:** Top- $K$  nearest neighbors  $\mathcal{N}_K$

- 1 Transform  $\mathbf{p}^T$  to  $\hat{\mathbf{p}}^G$  using  $\hat{X}^-$  (Eq. (3)).
- 2 Compute the global voxel index  $\mathbf{k}_p$ , obtain  $(b_x, b_y, b_z)$  and hence  $s_p$  via Eq. (4).
- 3 Let  $m^* = \max\{m \mid d_m \leq R\}$ ;
- 4 Set  $\mathcal{T}^* = [\mathcal{H}_0 \parallel \dots \parallel \mathcal{H}_{m^*}]$  and  $\mathcal{D}^* = \{d_0, \dots, d_{m^*}\}$ .
- 5 Initialize a bounded max-heap  $\mathbf{H}$  with capacity  $K$ .
- 6 **for**  $i \in [0, m^*]$  **do**
- 7   **if**  $|\mathbf{H}| = K$  **and**  $d_m > \text{maxdist}(\mathbf{H})$  **then break**;
- 8   **foreach**  $(k_x, k_y, k_z, s) \in \mathcal{H}_i$  **do**
- 9     // Eq. (9): octant reflection
- 10      $\sigma_x \leftarrow (-1)^{b_x}$ ,  $\sigma_y \leftarrow (-1)^{b_y}$ ,  $\sigma_z \leftarrow (-1)^{b_z}$
- 11      $\Delta\mathbf{k} \leftarrow (\sigma_x k_x, \sigma_y k_y, \sigma_z k_z)$
- 12      $\mathbf{k}' \leftarrow \mathbf{k} + \Delta\mathbf{k}$  and  $s' \leftarrow s \oplus s_p$
- 13      $\mu \leftarrow \mathcal{V}(\mathbf{k}', s')$
- 14      $\delta \leftarrow \|\hat{\mathbf{p}}^G - \mu\|_2$
- 15     **if**  $\delta > R$  **then continue**;
- 16     **if**  $|\mathbf{H}| < K$  **then** push  $(\delta, \mu)$  into  $\mathbf{H}$ ; **continue**;
- 17     **if**  $\delta < \text{maxdist}(\mathbf{H})$  **then**
- 18       pop worst from  $\mathbf{H}$ ; push  $(\delta, \mu)$  into  $\mathbf{H}$

18  $\mathcal{N}_K \leftarrow$  extract elements of  $\mathbf{H}$  in ascending order of  $\delta$ .

---

completing a group, if the heap is full and its worst distance  $r_K$  is strictly less than the lower bound of the next group, the search terminates. The lower-bound property of the grouping certifies that any unvisited candidate is no closer than that threshold and thus cannot reduce  $r_K$ . Together, these properties produce exact top- $K$  neighbors with geometric completeness while substantially reducing candidate evaluations.

The detailed procedure is summarized in Algorithm 1, where  $|\mathbf{H}|$  and  $\text{maxdist}(\mathbf{H})$  denote the number of elements in the max-heap  $\mathbf{H}$  and the largest distance among them, respectively.

### E. Discussion

We use PCA on neighboring points to fit local planes and form point-to-plane residuals, a formulation introduced in [7] and widely validated in subsequent LIO systems for stable performance. Our proposed map structure and the corresponding HKNN search are highly efficient for LiDAR SLAM and can be easily integrated into existing systems.

Compared with voxel-neighbor methods [15], enlarging the association range usually comes with high cost. Our HKNN offers better tolerance to the choice of  $R$  and yields more reliable neighbors in sparse scans, but excessively increasing  $R$  still introduces unnecessary overhead, especially in LiDAR-inertial odometry applications.

Empirically, the hyperparameter  $\tau_{\text{merge}}$  (Section III-C) is most effective for non-repetitive LiDARs, as it constrains the averaging range and mitigates single-shot noise, while its impact

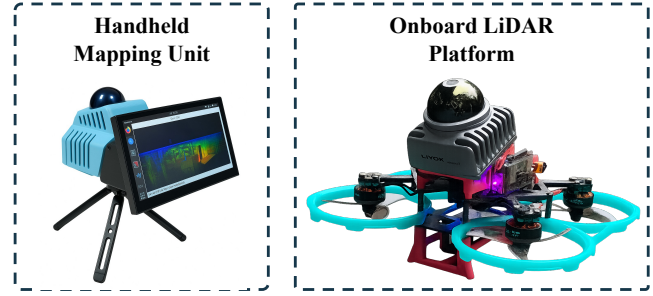


Fig. 4. Experimental platforms used for dataset collection. (Left) A handheld mapping unit equipped with a Livox-MID360 LiDAR, RGB camera, and an NVIDIA Orin NX embedded processor. (Right) A 220 mm quadrotor UAV carrying the same LiDAR and embedded processor, used for autonomous flight experiments.

on mechanical spinning LiDARs is minor. Setting it to about  $3\sigma$  of the noise is generally reasonable. We note this to guide users of our open-source implementation in parameter tuning; for all experiments in Section IV, we used the same configuration across sensors and environments.

## IV. EXPERIMENT

In this section, we evaluate the proposed Super-LIO system on two computing platforms, X86 and ARM, as well as on multiple datasets. We compare its performance against state-of-the-art lightweight LIO frameworks. The evaluation covers both accuracy and efficiency, with a particular emphasis on runtime performance under resource-constrained conditions. We further conduct robustness tests across a wide variety of real-world scenarios.

### A. Experimental Setup

We compare Super-LIO against several lightweight LiDAR-Inertial Odometry baselines, including **FAST-LIO2** [14], **Faster-LIO** [15], and **iG-LIO** [18]. To isolate the contribution of our HKNN strategy, we further implement an ablation variant, **Super-LIO\***, which is identical to Super-LIO but replaces HKNN with the 18-neighbor voxel search of Faster-LIO. In addition, we provide a concurrency-optimized version of FAST-LIO2, denoted as **FAST-LIO2\***, for fair real-time evaluation.

For fairness, all methods use identical parameter settings: maximum iterations = 4, random downsampling rate = 3, and voxel downsampling resolution = 0.5 m. For our method and other voxel-based approaches [15], [18], the map voxel size is also set to 0.5 m. The HKNN in Super-LIO is configured with  $R_{max} = 0.875$  m, covering a  $7 \times 7 \times 7$  subvoxel region that offers a larger search range than Super-LIO\* and Faster-LIO. Except for LiDAR-IMU extrinsic calibrations, which vary across datasets, all other parameters are kept at default values throughout the experiments.

Experiments are conducted on both public and private datasets. Public benchmarks include M2DGR [34], NCLT [35], MCD [36], and NTU [37], all with ground-truth trajectories for accuracy evaluation. Our private dataset comprises ten sequences covering diverse indoor and outdoor environments,

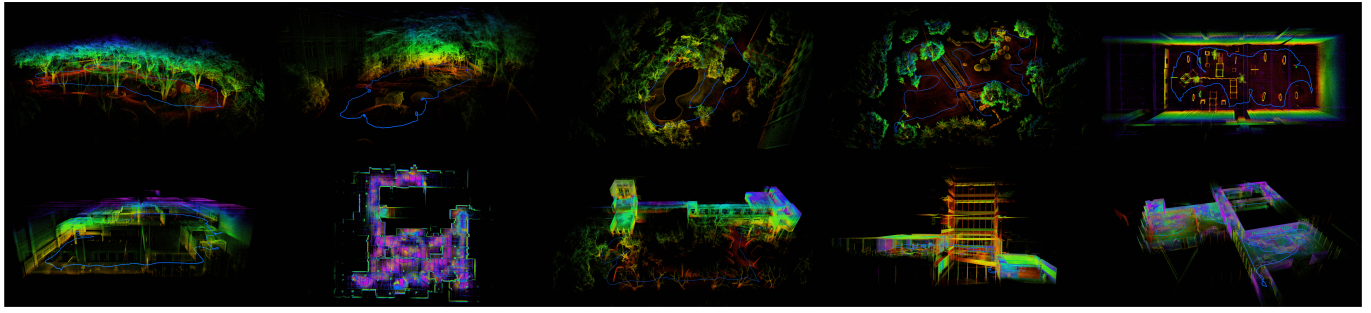


Fig. 5. Ten self-collected point cloud sequences deliberately selected to cover diverse environment dimensions—indoor vs. outdoor, structured vs. unstructured, and open vs. confined—including parks and ponds, forests, drone-racing arenas, factories, underground garages, and office spaces. The sequences are indexed from 01 to 10 in row-major order (left to right, top to bottom), where 04, 05, 07, and 09 are collected by autonomous UAV flights.

TABLE I  
RMSE (m) ON PUBLIC DATASETS (X86 @ 5× SPEED)

Seq.	Super-LIO	Super-LIO*	FAST-LIO2	FAST-LIO2*	Faster-LIO	iG-LIO	Dist.(km)
m2s1	0.38	0.40	0.38	<u>0.32</u>	<b>0.32</b>	0.33	0.75
m2s2	<b>2.80</b>	3.05	<u>2.86</u>	<u>2.89</u>	3.11	2.97	1.48
m2s3	<b>0.14</b>	<u>0.15</u>	0.20	0.20	0.17	0.20	0.42
m2s4	0.64	0.67	<u>0.45</u>	0.47	0.60	<b>0.43</b>	0.84
m2s5	0.38	0.39	0.38	<u>0.37</u>	0.39	<b>0.27</b>	0.42
m2h1	<b>0.29</b>	0.29	0.30	0.30	0.30	0.31	0.21
m2h5	<b>1.16</b>	<u>1.17</u>	1.20	1.20	1.19	1.17	0.29
m2d1	0.46	0.45	0.47	0.47	<u>0.45</u>	<b>0.44</b>	0.14
m2d2	<b>0.32</b>	0.34	0.36	0.36	<u>0.34</u>	0.37	0.06
nclt1	<b>1.69</b>	1.76	<u>1.72</u>	1.73	2.02	2.48	7.58
nclt2	<u>1.30</u>	1.32	1.42	1.48	1.32	<b>1.17</b>	3.19
nclt3	<b>1.82</b>	1.93	2.29	2.33	2.42	<u>1.88</u>	6.12
mcd0	<u>0.54</u>	0.63	<b>0.48</b>	0.57	0.57	1.29	3.20
mcd2	<b>0.72</b>	<u>0.79</u>	1.08	1.41	0.95	1.69	1.78
mcd3	<b>0.50</b>	<u>0.56</u>	0.58	<u>0.75</u>	<u>0.56</u>	0.92	1.46
mcd4	<b>0.60</b>	<u>0.63</u>	0.96	1.12	<u>0.70</u>	0.75	2.42
eee1	0.12	0.12	<b>0.08</b>	<u>0.08</u>	0.16	<b>X</b>	0.26
nyal	<u>0.07</u>	0.09	<b>0.06</b>	<b>0.06</b>	0.13	0.07	0.19
sbs1	<b>0.09</b>	0.09	0.09	0.09	0.13	0.09	0.22
Avg	<b>0.74</b>	<u>0.78</u>	0.81	0.85	0.83	0.93	1.63

The symbol **X** denotes a failed run. Styling rule: per row, all minima are **bold**; second-smallest distinct values are underlined. Ties share the same style.

used for runtime and robustness tests. All datasets are played at 5× real-time speed on the X86 platform to assess both throughput and accuracy, and at 1× speed on the Orin NX to evaluate real-time performance under resource constraints. Examples of private data collection platforms and sequences are shown in Fig. 4 and Fig. 5.

### B. Accuracy Evaluation

Accuracy is evaluated on public datasets with ground-truth trajectories, as introduced in Section IV-A. We use the Root Mean Square Error (RMSE) between estimated and ground-truth poses, computed by the Evo toolbox [38], as the evaluation metric.

For brevity, dataset names are simplified in Table I: for example, M2DGR sequences are denoted by the prefix “m2” and the NTU prefix is omitted in the last three rows. The same naming rule applies in the following analysis.

The evaluated datasets cover a wide spectrum of LiDAR types, platforms, and scenarios. M2DGR [34] and NCLT [35]

both employ a Velodyne HDL-32E spinning LiDAR. M2DGR consists of low-speed ground-robot runs, where we evaluate outdoor street and indoor corridor scenes. NCLT provides long-duration trajectories (up to 110 minutes and 7.58 km), allowing us to assess accuracy under extended continuous operation. The MCD [36] dataset uses a Livox MID-70 solid-state LiDAR with a small FoV, recorded on a high-speed terrain vehicle; the tested sequences exceed 1 km, with peak speed ~10 m/s and angular velocity ~2.9 rad/s, stressing both robustness and accuracy under fast motion. Finally, the NTU [37] dataset is collected with a UAV equipped with an Ouster-16 LiDAR, yielding relatively sparse aerial point clouds; this setting is particularly challenging, and iG-LIO [18] fails on one sequence (eee1).

Table I reports the RMSE results across multiple sequences. Super-LIO achieves the best average accuracy among all tested methods, despite relying on a significantly more compact map representation. In several sequences, it even surpasses state-of-the-art baselines, demonstrating the effectiveness of the OctVox map. The ablation variant Super-LIO\* shows a modest yet expected degradation, confirming that the proposed HKNN search improves the data association quality during scan-to-map alignment. By contrast, FAST-LIO2\* [14] exhibits a slight accuracy drop compared with FAST-LIO2 [14], which is mainly attributed to more aggressive multi-threading that introduces small numerical inconsistencies in scan-to-map optimization. While accuracy is important, the focus of this work is on optimizing efficiency, as discussed in the following sections.

### C. Efficiency Analysis

To evaluate runtime efficiency, we measure both per-frame processing time and CPU usage on the X86 laptop and the embedded NVIDIA Orin NX. In addition to public datasets, we introduce ten representative self-collected sequences, denoted with the prefix “se” for efficiency and robustness evaluation. These sequences are captured with a Livox MID-360 LiDAR, which employs a non-repetitive scanning pattern. Due to its lightweight design, this sensor is well suited for small-scale platforms such as UAVs, making the collected datasets more practically relevant.

Figure 1 provides an overview of average processing time and CPU utilization across methods, while Table II reports detailed results for each sequence, including per-frame processing time

TABLE II  
PER-FRAME RUNTIME STATISTICS ON X86 (AMD 5800H, 5× PLAYBACK) AND ARM (CORTEX-A78AE), IN MILLISECONDS

Seq	Super-LIO				Super-LIO*				FAST-LIO2				FAST-LIO2*				Faster-LIO				iG-LIO			
	x86		ARM		x86		ARM		x86		ARM		x86		ARM		x86		ARM		x86		ARM	
	Avg	Std	Avg	Std	Avg	Std	Avg	Std	Avg	Std	Avg	Std	Avg	Std	Avg	Std	Avg	Std	Avg	Std	Avg	Std	Avg	Std
m2s1	<b>4.94</b>	<b>1.31</b>	<b>19.18</b>	<b>2.33</b>	<b>5.85</b>	<u>1.63</u>	21.46	2.67	19.72	3.78	93.28	7.43	8.84	<u>1.63</u>	30.51	<b>2.62</b>	14.55	2.71	45.58	6.39	7.37	2.60	20.89	3.51
m2s2	<b>4.38</b>	<b>1.23</b>	<b>16.97</b>	<u>3.19</u>	<b>5.01</b>	<u>1.52</u>	<b>18.42</b>	<b>2.94</b>	17.77	3.52	77.26	12.98	7.83	<u>1.76</u>	27.61	<b>3.96</b>	12.77	2.48	37.07	4.26	7.20	2.46	21.45	3.60
m2s3	<b>5.20</b>	<b>1.19</b>	<b>20.01</b>	2.93	<b>6.21</b>	1.42	<u>21.17</u>	<b>2.91</b>	24.66	2.53	92.78	9.05	9.46	<u>1.21</u>	30.57	<b>2.84</b>	18.33	3.65	44.39	6.29	8.25	2.15	<b>X</b>	<b>X</b>
m2s4	<b>4.75</b>	<b>1.54</b>	<b>20.35</b>	<b>2.66</b>	<u>5.28</u>	<u>1.55</u>	21.95	<u>2.67</u>	19.68	4.10	93.85	5.25	8.26	<u>1.66</u>	30.48	2.74	13.27	3.27	42.62	4.24	6.95	2.61	<u>21.57</u>	4.49
m2s5	<b>4.46</b>	<u>1.40</u>	<b>15.36</b>	4.02	<u>4.67</u>	<b>1.38</b>	<u>16.22</u>	4.31	17.23	3.89	66.52	12.87	7.87	1.88	25.99	<u>3.39</u>	11.19	2.21	34.17	4.24	6.20	1.92	<u>19.92</u>	<b>3.32</b>
m2h1	<b>2.85</b>	<b>0.99</b>	<b>10.16</b>	<b>2.69</b>	<u>3.23</u>	<u>1.09</u>	<u>11.25</u>	2.90	11.89	1.65	45.72	4.39	6.81	1.90	22.77	<b>2.81</b>	12.15	2.68	30.26	4.06	5.52	1.37	<b>X</b>	<b>X</b>
m2h5	<b>2.55</b>	<b>0.88</b>	<b>9.58</b>	<b>2.63</b>	<u>3.62</u>	<u>1.05</u>	<u>11.16</u>	3.03	10.65	1.84	43.49	3.85	6.37	1.75	22.38	<u>2.73</u>	11.53	2.62	29.01	3.66	4.89	1.40	<b>X</b>	<b>X</b>
m2d1	<b>2.81</b>	<b>1.05</b>	<b>11.69</b>	<b>3.62</b>	<u>3.23</u>	<u>1.07</u>	<u>12.47</u>	3.90	11.24	3.04	50.12	11.03	6.43	1.88	22.90	<u>3.76</u>	10.31	1.89	29.46	4.55	4.68	1.48	<b>X</b>	<b>X</b>
m2d2	<b>2.97</b>	<b>1.10</b>	<b>10.74</b>	<b>3.28</b>	<u>3.35</u>	<u>1.15</u>	<u>11.69</u>	3.88	10.81	2.16	46.20	10.04	6.51	<u>1.97</u>	22.12	<u>3.37</u>	8.26	<u>1.67</u>	28.47	3.89	4.72	1.40	15.03	3.54
nclt1	<b>4.25</b>	<b>1.60</b>	<b>7.97</b>	<b>3.02</b>	<u>5.30</u>	<u>1.91</u>	<u>9.81</u>	3.63	13.27	4.64	31.01	8.34	7.29	2.26	14.09	<u>4.07</u>	9.82	2.95	15.45	4.53	5.92	2.98	<b>X</b>	<b>X</b>
nclt2	<b>4.20</b>	<b>1.51</b>	<b>9.06</b>	<b>3.13</b>	<u>4.99</u>	<u>1.79</u>	<u>10.84</u>	3.97	13.85	3.01	34.86	9.67	7.48	2.21	15.64	<u>4.46</u>	9.96	2.44	17.93	5.07	6.02	2.32	<b>X</b>	<b>X</b>
nclt3	<b>4.14</b>	<b>1.60</b>	<b>10.88</b>	<b>2.95</b>	<u>5.15</u>	<u>1.64</u>	<u>12.38</u>	3.26	13.48	37.15	42.75	8.11	7.19	2.19	19.97	3.91	9.92	3.06	23.98	4.53	5.37	2.15	<b>X</b>	<b>X</b>
mcd0	<b>1.59</b>	<b>1.00</b>	<b>6.07</b>	<b>1.62</b>	<u>1.97</u>	1.34	<u>8.68</u>	<u>2.06</u>	5.37	1.26	20.60	4.69	3.06	<u>1.17</u>	10.38	3.09	3.12	1.36	10.55	<b>2.97</b>	2.98	1.47	<b>X</b>	<b>X</b>
mcd2	<b>1.84</b>	<b>0.92</b>	<b>7.06</b>	<u>2.27</u>	<u>2.31</u>	<u>0.94</u>	<u>7.30</u>	<b>1.97</b>	5.59	1.52	24.66	5.64	3.09	1.16	11.24	2.82	3.37	1.94	12.40	4.07	3.05	1.84	<b>X</b>	<b>X</b>
mcd3	<b>1.84</b>	<b>0.89</b>	<b>7.22</b>	<b>1.63</b>	<u>2.10</u>	<u>0.93</u>	<u>7.61</u>	<u>2.47</u>	5.51	1.39	23.80	5.11	3.03	1.17	11.05	2.91	3.14	1.13	12.38	3.32	3.17	1.85	<b>X</b>	<b>X</b>
mcd4	<b>1.65</b>	<b>0.77</b>	<b>5.86</b>	<b>2.25</b>	<u>1.95</u>	<u>0.89</u>	<u>6.83</u>	<u>3.24</u>	5.52	1.53	22.04	6.11	3.11	1.22	10.87	<u>3.25</u>	3.16	<u>1.59</u>	11.26	<u>3.59</u>	3.15	<u>7.43</u>	<b>X</b>	<b>X</b>
eee1	<b>3.22</b>	<b>1.11</b>	<b>9.91</b>	<b>2.73</b>	<u>3.68</u>	<u>1.24</u>	<u>10.16</u>	<u>4.06</u>	10.54	2.33	33.84	11.84	5.47	1.59	14.37	4.47	9.38	2.65	17.79	<u>7.09</u>	<b>X</b>	<b>X</b>	<b>X</b>	<b>X</b>
nya1	<b>2.44</b>	<b>0.96</b>	<b>7.15</b>	<b>1.94</b>	<u>2.69</u>	<u>1.10</u>	<u>8.84</u>	<u>2.59</u>	8.00	1.75	23.19	6.33	4.85	1.56	12.16	3.72	8.20	2.63	13.64	4.73	3.66	1.16	<b>X</b>	<b>X</b>
sbs1	<b>2.74</b>	<b>1.06</b>	<b>8.77</b>	<b>2.67</b>	3.08	<u>1.10</u>	<u>10.53</u>	<u>3.90</u>	8.32	1.84	30.16	8.73	4.84	1.51	12.93	4.22	7.39	1.88	16.32	6.52	3.78	1.30	<b>X</b>	<b>X</b>
se01	<b>3.20</b>	1.23	<b>13.69</b>	<b>3.16</b>	<u>3.30</u>	<b>1.15</b>	<u>16.09</u>	3.35	11.10	1.61	52.33	6.50	5.24	<u>1.19</u>	19.64	4.08	7.14	1.30	26.33	3.54	4.84	1.75	<b>X</b>	<b>X</b>
se02	<b>2.76</b>	<b>1.00</b>	<b>9.99</b>	<b>2.98</b>	<u>2.87</u>	<u>1.03</u>	<u>13.17</u>	<u>3.27</u>	9.42	1.88	40.56	5.91	4.91	1.33	15.56	<u>3.46</u>	6.50	1.53	21.94	3.31	3.96	1.42	<b>X</b>	<b>X</b>
se03	<b>2.53</b>	<b>0.94</b>	<b>9.14</b>	<b>2.10</b>	<u>2.68</u>	<u>0.96</u>	<u>12.77</u>	2.73	8.74	1.42	38.43	3.45	5.13	1.46	15.57	<u>2.52</u>	6.14	1.50	21.11	2.71	3.85	1.44	<b>X</b>	<b>X</b>
se04	<b>0.76</b>	<u>0.33</u>	<b>3.81</b>	<b>1.91</b>	<u>0.80</u>	<b>0.32</b>	<u>4.72</u>	<u>2.47</u>	2.99	0.91	15.89	6.40	1.73	0.68	6.62	2.78	2.54	0.87	8.65	2.84	1.67	0.63	<b>X</b>	<b>X</b>
se05	<b>1.07</b>	<b>0.47</b>	<b>4.79</b>	<b>2.14</b>	<u>1.12</u>	<u>0.48</u>	<u>5.72</u>	<u>2.61</u>	4.50	1.53	19.91	6.45	2.62	1.07	9.20	2.85	3.12	1.20	11.67	3.16	2.19	0.92	8.21	2.90
se06	<b>0.75</b>	<u>0.36</u>	<b>3.22</b>	<b>1.47</b>	<b>0.74</b>	<b>0.34</b>	<u>4.45</u>	<u>1.70</u>	3.09	1.30	14.32	6.69	1.97	0.87	6.79	<u>2.67</u>	2.35	1.12	8.47	3.36	1.67	0.71	<b>X</b>	<b>X</b>
se07	<b>1.16</b>	<b>0.46</b>	<b>4.99</b>	<b>1.35</b>	<u>1.18</u>	<b>0.46</b>	<u>5.92</u>	<u>1.77</u>	5.43	1.42	25.36	4.62	3.63	1.44	12.17	3.22	4.23	1.65	14.35	3.00	2.61	<u>1.00</u>	<b>X</b>	<b>X</b>
se08	<b>0.69</b>	<b>0.45</b>	<b>2.19</b>	<b>1.19</b>	<u>0.72</u>	<u>0.46</u>	<u>2.83</u>	<u>1.58</u>	3.26	2.10	9.06	3.65	2.07	1.27	5.65	2.48	2.74	1.43	7.34	<u>2.63</u>	<b>X</b>	<b>X</b>	<b>X</b>	<b>X</b>
se09	<b>0.69</b>	<u>0.27</u>	<b>3.54</b>	<b>1.83</b>	<u>0.74</u>	<b>0.26</b>	<u>4.16</u>	2.08	3.07	0.91	15.54	4.56	1.88	0.63	6.84	<u>1.84</u>	2.41	0.83	8.93	2.31	1.56	0.57	<b>X</b>	<b>X</b>
se10	<b>0.64</b>	<u>0.33</u>	<b>3.25</b>	<u>1.48</u>	<b>0.63</b>	<b>0.31</b>	<u>3.29</u>	<b>1.33</b>	3.01	1.64	14.60	5.93	2.18	1.23	7.32	<u>2.74</u>	2.59	1.38	9.56	3.41	<b>X</b>	<b>X</b>	<b>X</b>	<b>X</b>
AVG	<b>2.66</b>	<b>0.96</b>	<b>9.40</b>	<b>2.45</b>	<u>3.05</u>	<b>1.05</b>	<u>10.75</u>	<b>2.87</b>	9.92	3.37	39.38	7.09	5.14	1.48	16.32	3.23	7.57	1.99	21.07	4.08	4.43	1.86	17.85	3.56
RATE	1x	1x	1x	1x	1.2x	1.1x	1.1x	1.2x	3.7x	3.5x	4.2x	2.9x	1.9x	1.5x	1.7x	1.3x	2.9x	2.1x	2.2x	1.7x	1.8x	1.9x	1.9x	1.6x

and standard deviation on both X86 and ARM platforms. From these results, Super-LIO achieves a clear efficiency advantage: it consumes fewer CPU resources than FAST-LIO2 on both platforms, while delivering 3.7× and 4.2× speedups on X86 and ARM, respectively, demonstrating its consistent advantage across platforms.

$$\eta = \frac{1}{N} \sum_{i=1}^N \frac{1}{t_i \cdot u_i}$$

where  $t_i$  denotes the per-frame processing time measured in milliseconds and  $u_i$  represents the normalized CPU utilization (0–1), balancing frame rate against computational cost. Based on this definition, Table III summarizes the relative efficiency of all methods on both the X86 and ARM platforms. Super-LIO delivers 2.4× and 1.61× the relative efficiency of iG-LIO on X86 and ARM, respectively, demonstrating its consistent advantage across platforms.

#### D. Robustness Analysis

Our self-collected dataset covers diverse and challenging scenarios. In UAV sequences, the maximum linear velocity reaches 4.95 m/s, the maximum angular velocity is 4.33 rad/s, and the longest trajectory extends to 645 m. Indoor runs include narrow corridors with widths below 1.5 m, which are particularly demanding for real-time LiDAR-inertial odometry. Across all sequences, Super-LIO consistently maintains stable performance.

Combined with the evaluations on public datasets, featuring high-speed motion, long-duration trajectories, diverse indoor and outdoor scenes, and sparse aerial point clouds, these results demonstrate that Super-LIO achieves robust and reliable performance under a wide spectrum of real-world operating conditions.

We also rigorously evaluated performance across both X86 and ARM platforms, confirming the cross-platform consistency of Super-LIO, as shown in Table II. In contrast, although iG-

TABLE III  
RELATIVE EFFICIENCY ↑ ON X86 AND ARM PLATFORMS.

	Super-LIO	Super-LIO*	FAST-LIO2	FAST-LIO2*	Faster-LIO	iG-LIO
X86	<b>1.99</b>	<u>1.56</u>	0.42	0.66	0.30	0.83
ARM	<b>1.71</b>	<u>1.37</u>	0.39	0.66	0.40	1.06

LIO delivers competitive real-time performance and accuracy on X86, it frequently fails on ARM.

## V. CONCLUSION

We have introduced Super-LIO, a LiDAR-inertial odometry system that combines accuracy, efficiency, and robustness. Its design relies on two lightweight modules: OctVox for compact octo-voxel mapping and HKNN for fast and reliable KNN search. Extensive evaluations on public benchmarks and challenging self-collected datasets show consistently higher efficiency without compromising accuracy or robustness, including in high-speed, long-duration, sparse-sensing, and narrow-scene scenarios. Tests on both X86 and ARM platforms further validate stable performance and suitability for embedded deployment.

Super-LIO will be released as open source and is intended as a practical, integrable solution for robotic applications with strict compute and power limitations.

## REFERENCES

- [1] B. Zhou, J. Yi, X. Zhang, L. Wang, S. Zhang, and B. Wu, “An autonomous navigation approach for unmanned vehicle in off-road environment with self-supervised traversal cost prediction,” *Applied Intelligence*, vol. 53, no. 17, pp. 20 091–20 109, 2023.
- [2] Y. Ren, F. Zhu, G. Lu, Y. Cai, L. Yin, F. Kong, J. Lin, N. Chen, and F. Zhang, “Safety-assured high-speed navigation for mavs,” *Science Robotics*, vol. 10, no. 98, p. eado6187, 2025.
- [3] Y. Li and J. Ibanez-Guzman, “Lidar for autonomous driving: The principles, challenges, and trends for automotive lidar and perception systems,” *IEEE Signal Processing Magazine*, vol. 37, no. 4, pp. 50–61, 2020.
- [4] S. Geng, Z. Ning, F. Zhang, and B. Zhou, “Epic: A lightweight lidar-based uav exploration framework for large-scale scenarios,” *IEEE Robotics and Automation Letters*, 2025.
- [5] Y. Gao, C. Li, Z. You, J. Liu, Z. Li, P. Chen, Q. Chen, Z. Tang, L. Wang, P. Yang *et al.*, “Openfly: A comprehensive platform for aerial vision-language navigation,” *arXiv preprint arXiv:2502.18041*, 2025.
- [6] X. Zhou, X. Wen, Z. Wang, Y. Gao, H. Li, Q. Wang, T. Yang, H. Lu, Y. Cao, C. Xu *et al.*, “Swarm of micro flying robots in the wild,” *Science Robotics*, vol. 7, no. 66, p. eabm5954, 2022.
- [7] J. Zhang and S. Singh, “Loam: Lidar odometry and mapping in real-time,” *Robotics: Science and Systems*, vol. 2, no. 9, pp. 1–9, 2015.
- [8] T. Shan and B. Englot, “Lego-loam: Lightweight and ground-optimized lidar odometry and mapping on variable terrain,” in *2018 IEEE/RSJ International Conference on Intelligent Robots and Systems (IROS)*. IEEE, 2018, pp. 4758–4765.
- [9] T. Shan, B. Englot, D. Meyers, W. Wang, C. Ratti, and D. Rus, “Lio-sam: Tightly-coupled lidar inertial odometry via smoothing and mapping,” in *2020 IEEE/RSJ international conference on intelligent robots and systems (IROS)*. IEEE, 2020, pp. 5135–5142.
- [10] F. Dellaert, “Factor graphs and gtsam: A hands-on introduction,” *Georgia Institute of Technology, Tech. Rep.*, vol. 2, no. 4, 2012.
- [11] X. Liu, Z. Liu, F. Kong, and F. Zhang, “Large-scale lidar consistent mapping using hierarchical lidar bundle adjustment,” *IEEE Robotics and Automation Letters*, vol. 8, no. 3, pp. 1523–1530, 2023.
- [12] Z. Liu, H. Li, C. Yuan, X. Liu, J. Lin, R. Li, C. Zheng, B. Zhou, W. Liu, and F. Zhang, “Voxel-slam: A complete, accurate, and versatile lidar-inertial slam system,” *arXiv preprint arXiv:2410.08935*, 2024.
- [13] W. Xu and F. Zhang, “Fast-lio: A fast, robust lidar-inertial odometry package by tightly-coupled iterated kalman filter,” *IEEE Robotics and Automation Letters*, vol. 6, no. 2, pp. 3317–3324, 2021.
- [14] W. Xu, Y. Cai, D. He, J. Lin, and F. Zhang, “Fast-lio2: Fast direct lidar-inertial odometry,” *IEEE Transactions on Robotics*, vol. 38, no. 4, pp. 2053–2073, 2022.
- [15] C. Bai, T. Xiao, Y. Chen, H. Wang, F. Zhang, and X. Gao, “Faster-lio: Lightweight tightly coupled lidar-inertial odometry using parallel sparse incremental voxels,” *IEEE Robotics and Automation Letters*, vol. 7, no. 2, pp. 4861–4868, 2022.
- [16] D. He, W. Xu, N. Chen, F. Kong, C. Yuan, and F. Zhang, “Point-lio: Robust high-bandwidth light detection and ranging inertial odometry,” *Advanced Intelligent Systems*, vol. 5, no. 7, p. 2200459, 2023.
- [17] C. Yuan, W. Xu, X. Liu, X. Hong, and F. Zhang, “Efficient and probabilistic adaptive voxel mapping for accurate online lidar odometry,” *IEEE Robotics and Automation Letters*, vol. 7, no. 3, pp. 8518–8525, 2022.
- [18] Z. Chen, Y. Xu, S. Yuan, and L. Xie, “ig-lio: An incremental gicp-based tightly-coupled lidar-inertial odometry,” *IEEE Robotics and Automation Letters*, 2024.
- [19] K. Koide, M. Yokozuka, S. Oishi, and A. Banno, “Voxelized gicp for fast and accurate 3d point cloud registration,” in *2021 IEEE International Conference on Robotics and Automation (ICRA)*. IEEE, 2021, pp. 11 054–11 059.
- [20] R. Xiao, W. Liu, Y. Chen, and L. Hu, “Liv-gs: Lidar-vision integration for 3d gaussian splatting slam in outdoor environments,” *IEEE Robotics and Automation Letters*, 2024.
- [21] S. Hong, C. Zheng, Y. Shen, C. Li, F. Zhang, T. Qin, and S. Shen, “Gslivo: Real-time lidar, inertial, and visual multi-sensor fused odometry with gaussian mapping,” *arXiv preprint arXiv:2501.08672*, 2025.
- [22] T.-M. Nguyen, D. Duberg, P. Jensfelt, S. Yuan, and L. Xie, “Slict: Multi-input multi-scale surfel-based lidar-inertial continuous-time odometry and mapping,” *IEEE Robotics and Automation Letters*, vol. 8, no. 4, pp. 2102–2109, 2023.
- [23] J. Sola, “Quaternion kinematics for the error-state kalman filter,” *arXiv preprint arXiv:1711.02508*, 2017.
- [24] C. Zhang, J. Zhang, Q. Liu, Y. Liu, and J. Qin, “Si-lio: High-precision tightly-coupled lidar-inertial odometry via single-iteration invariant extended kalman filter,” *IEEE Robotics and Automation Letters*, 2024.
- [25] A. Barrau and S. Bonnabel, “The invariant extended kalman filter as a stable observer,” *IEEE Transactions on Automatic Control*, vol. 62, no. 4, pp. 1797–1812, 2016.
- [26] J. Zhu, H. Li, Z. Wang, S. Wang, and T. Zhang, “i-octree: A fast, lightweight, and dynamic octree for proximity search,” in *2024 IEEE International Conference on Robotics and Automation (ICRA)*. IEEE, 2024, pp. 12 290–12 296.
- [27] D. Duberg and P. Jensfelt, “Ufomap: An efficient probabilistic 3d mapping framework that embraces the unknown,” *IEEE Robotics and Automation Letters*, vol. 5, no. 4, pp. 6411–6418, 2020.
- [28] I. Vizzo, T. Guadagnino, B. Mersch, L. Wiesmann, J. Behley, and C. Stachniss, “Kiss-icp: In defense of point-to-point icp-simple, accurate, and robust registration if done the right way,” *IEEE Robotics and Automation Letters*, vol. 8, no. 2, pp. 1029–1036, 2023.
- [29] C. Zhao, K. Hu, J. Xu, L. Zhao, B. Han, K. Wu, M. Tian, and S. Yuan, “Adaptive-lio: Enhancing robustness and precision through environmental adaptation in lidar inertial odometry,” *IEEE Internet of Things Journal*, 2024.
- [30] K. Koide, M. Yokozuka, S. Oishi, and A. Banno, “Glim: 3d range-inertial localization and mapping with gpu-accelerated scan matching factors,” *Robotics and Autonomous Systems*, vol. 179, p. 104750, 2024.
- [31] K. Chen, R. Nemiroff, and B. T. Lopez, “Direct lidar-inertial odometry: Lightweight lio with continuous-time motion correction,” in *2023 IEEE international conference on robotics and automation (ICRA)*. IEEE, 2023, pp. 3983–3989.
- [32] P. Celis, P.-A. Larson, and J. I. Munro, “Robin hood hashing,” in *26th annual symposium on foundations of computer science (sfcs 1985)*. IEEE, 1985, pp. 281–288.
- [33] Tessil, “robin-map: A c++ implementation of a fast hash map and hash set using robin hood hashing,” <https://github.com/Tessil/robin-map>, 2025, version 1.4.0, MIT License.
- [34] X. Yin, S. Hu, Z. Xiong, Z. Chen, Y. Liu, X. Huang, J. Zhang, W. Li, M. Tan, Q. Wang *et al.*, “M2dgr: A multi-sensor and multi-scenario slam dataset for ground robots,” *arXiv preprint arXiv:2107.11181*, 2021.
- [35] N. Carlevaris-Bianco, A. Ushani, and R. M. Eustice, “University of michigan north campus long-term vision and lidar dataset,” *International Journal of Robotics Research (IJRR)*, vol. 35, no. 9, pp. 1023–1035, 2016.
- [36] T.-M. Nguyen, S. Yuan, T. H. Nguyen, P. Yin, H. Cao, L. Xie, M. Wozniak, P. Jensfelt, M. Thiel, J. Ziegenebein *et al.*, “Mcd: Diverse large-scale multi-campus dataset for robot perception,” in *Proceedings of the IEEE/CVF Conference on Computer Vision and Pattern Recognition*, 2024, pp. 22 304–22 313.
- [37] T.-M. Nguyen, S. Yuan, M. Cao, Y. Lyu, T. H. Nguyen, and L. Xie, “Ntu viral: A visual-inertial-ranging-lidar dataset, from an aerial vehicle viewpoint,” *The International Journal of Robotics Research*, vol. 41, no. 3, pp. 270–280, 2022.
- [38] M. Grupp, “evo: Python package for the evaluation of odometry and slam.” <https://github.com/MichaelGrupp/evo>, 2017.